Nano-Micro Letters

e-ISSN 2150-5551
CN 31-2103/TB

ARTICLE

https://doi.org/10.1007/s40820-026-02085-z

Engineering PtFe/LiO$_2$ Frontier Orbital Interaction in Li–O$_2$ Batteries

Cite as
Nano-Micro Lett.
(2026) 18:257

Received: 10 October 2025
Accepted: 29 December 2025

Yin Zhou[1], Kun Yin[2], Tian Zhang[1], Dongyu Feng[1], Jiapei Li[1], Anquan Zhu[1], Dewu Lin[1], Pan Xue[1], Yu Liu[1], Yongyu Liu[1], Kai Liu[1], Kunlun Liu[1], Chuhao Luan[1], Huawei Yang[2], Hou Chen[2], Yagang Yao[3], Guo Hong[1,4] ✉

HIGHLIGHTS

- PtFe catalyst was rationally designed based on frontier molecular orbital theory to investigate orbital-level interactions for enhanced oxygen evolution reaction activity in Li–O$_2$ batteries.
- The $d_z{}^2$–$d_z{}^2$ orbital coupling between Fe and Pt leads to electron donation from Fe to Pt, increasing electron population in the Pt $d_z{}^2$ orbital.
- Excess electrons from the Pt $d_z{}^2$ orbital occupy antibonding states with LiO$_2$, weakening interaction strength and boosting oxygen evolution reaction kinetics.

ABSTRACT Elucidating the structure–activity relationship between the electronic structure of catalytic active sites and oxygen evolution reaction (OER) activity at the orbital level is critical *yet* challenging in lithium–oxygen (Li–O$_2$) batteries. Herein, employing frontier molecular orbital theory, we designed a Pt-based catalyst as a model cathode to investigate the influence of frontier orbital interactions between the Pt $d_z{}^2$ orbital and the 5σ orbital of LiO$_2$ on the OER activity. Specifically, compared to the pure Pt catalyst, the $d_z{}^2$–$d_z{}^2$ orbital coupling between low-electronegativity Fe and Pt in PtFe catalyst induces predominant electron transfer from Fe to the $d_z{}^2$ frontier orbital of Pt. As the Pt content in PtFe alloys increases progressively (from Pt$_{58}$Fe$_{42}$, Pt$_{67}$Fe$_{33}$ to Pt$_{76}$Fe$_{24}$), the electron population of the Pt 5$d_z{}^2$ orbital gradually decreases (1.92 for Pt$_{58}$Fe$_{42}$, 1.85 for Pt$_{67}$Fe$_{33}$, and 1.80 for Pt$_{76}$Fe$_{24}$). This leads to a gradual enhancement in the strength of interactions between the Pt $d_z{}^2$ orbital and the frontier orbitals of LiO$_2$, consequently resulting in a progressive decline in the OER catalytic activity. Establishing the correlating between the electron population in the $d_z{}^2$ frontier orbital and OER activity provides a descriptor for designing efficient electrocatalysts in Li–O$_2$ batteries.

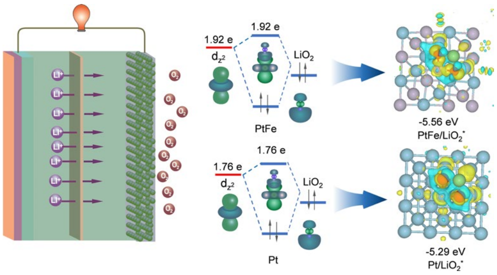

KEYWORDS Lithium–oxygen batteries; Frontier orbital; OER descriptor; Energy barrier

---

Yin Zhou, Kun Yin, and Tian Zhang have contributed equally to this work.

✉ Guo Hong, guohong@cityu.edu.hk
[1] Department of Materials Science and Engineering & Center of Super-Diamond and Advanced Films, City University of Hong Kong, 83 Tat Chee Avenue, Kowloon 999077, Hong Kong SAR, People's Republic of China
[2] School of Chemistry and Materials Science, Shandong Key University Laboratory of High Performance and Functional Polymer, Ludong University, Yantai 264025, People's Republic of China
[3] National Laboratory of Solid State Microstructures, College of Engineering and Applied Sciences, Jiangsu Key Laboratory of Artificial Functional Materials, Collaborative Innovation Center of Advanced Microstructures, Nanjing University, Nanjing 210093, People's Republic of China
[4] The Shenzhen Research Institute, City University of Hong Kong, Shenzhen 518057, People's Republic of China

Shanghai Jiao Tong University Press

Springer

1 Introduction

Lithium–oxygen (Li–O_2) batteries have recently gained widespread attentions due to the extremely high energy density (3500 Wh kg^{-1}) [1–6]. However, the sluggish oxygen evolution reactions (OER) kinetics during the charging process of Li–O_2 batteries result in low energy efficiency and high charging overpotential [7–12]. Although conventional redox mediators, e.g., triarylmethyl cations [13], can significantly improve OER kinetics, the shuttling effect and the inherent thermodynamic instability of liquid-phase catalysts lead to an inferior lifespan [13–16]. In contrast, various solid-phase catalysts such as noble metals [17–19], high-entropy alloys [20, 21], transition metal oxides [22–24], sulfides [25–27], single atoms [28–33], MXenes [34–36], etc. are widely employed as the catalytic alternatives for the enhanced fast OER process. Due to the direct correlation between *d*-orbital characteristics and catalytic activity, *d*-band center theory has been widely accepted as a descriptor for *d*-orbital electronic state, enabling rational design of high-performance catalysts by orbital hybridization [37, 38], and orbital coupling [39, 40]. However, as only a statistical average of the d-electron density of states, the *d*-band center cannot reveal the true electronic structure of active sites at specific energy levels and thus cannot precisely resolve the differential influence of site-specific *d*-orbital electron occupation on the OER catalytic activity.

Herein, unlike the *d*-band center theory, we utilize frontier orbital theory and construct Pt-based catalyst as a model platform to investigate the influence of frontier orbital interactions between Pt d_z^2 orbital and 5σ orbital of LiO_2 on OER activity. The selection of PtFe as the cathode catalyst for Li–O_2 batteries is guided by three fundamental mechanistic considerations. First, the interaction between Fe and Pt induces lattice strain effects that accurately modulate the Pt *d*-band center and regulate electron back-donation. This leads to optimized adsorption of oxygen intermediates such as LiO_2*, thereby accelerating the OER kinetics. Second, the incorporation of Fe significantly enhances the stability of Pt by preventing its dissolution and aggregation under strongly oxidative conditions. At the same time, it facilitates high utilization of Pt through atomic-scale dispersion. Third, the catalytic performance of PtFe systems has been well demonstrated in various oxygen-related reactions, including oxygen reduction reaction in fuel cells and OER in water electrolysis. These prior studies provide a strong theoretical and experimental basis for the rational design and mechanistic application of PtFe catalysts in Li–O_2 battery systems. In the PtFe system, the intrinsic *d*–*d*-orbital interaction between Fe and Pt enables precise modulation of the electron occupancy in the Pt d_z^2 orbital at the active site. This, in turn, allows for fine-tuning of the binding strength between the active site and reaction intermediates (such as LiO_2*), thereby effectively regulating the OER activity. Therefore, when d_z^2 frontier orbital of Pt in PtFe interacts with the 5σ orbital of LiO_2, the excess electrons in the Pt d_z^2 orbital occupy the antibonding orbital, thereby weakening the adsorption of LiO_2 and ultimately improving the OER catalytic activity. It is worth noting that the frontier orbital theory-based regulation strategy we employ differs from conventional hybridization engineering. Hybridization engineering is primarily based on the *d*-band center theory. However, the *d*-band center fails to capture the detailed electronic structure of active sites at specific energy levels and therefore cannot accurately elucidate the role of electron occupancy in individual *d*-orbitals on OER catalytic activity. In contrast, frontier orbital theory enables a more precise understanding of how specific *d*-orbital components contribute to OER performances. This work establishes a correlation between the electron number of d_z^2 frontier orbital and OER catalytic activity, which provides a descriptor for designing high-performance Li–O_2 batteries.

2 Experimental Section

2.1 Materials

Platinum(II) acetylacetonate ($Pt(acac)_2$, ≥ 99.99%), iron(III) acetylacetonate (acetylacetonate ($Fe(acac)_3$, ≥ 98%), Glucose (≥ 98%), hexadecyl trimethyl ammonium bromide (≥ 99%), poly(vinylidene fluoride) (PVDF), Li anode (lithium foil), lithium trifluoromethanesulfonate ($LiCF_3SO_3$, ≥ 99.5%) were purchased from Aladdin. Oleylamine ($C_{18}H_{37}N$, 80%-90%), cyclohexane (C_6H_{12}, ≥ 99.9%), ethanol solvent (C_2H_5OH, ≥ 99.7%), acetic acid (CH_3COOH, ≥ 99.5%), 1-methyl-2 pyrrolidone (NMP, $C_6H_{13}NO$, ≥ 99.5%), tetraethylene glycol dimethyl ether ($C_{10}H_{22}O_5$, 99%) were obtained from Macklin.

https://doi.org/10.1007/s40820-026-02085-z

2.2 Synthesis of PtFe ($Pt_{58}Fe_{42}$, $Pt_{67}Fe_{33}$, and $Pt_{76}Fe_{24}$) Nanowires

Dissolve 10 mg platinum(II) acetylacetonate ($Pt(acac)_2$), 3.6 mg iron(III) acetylacetonate ($Fe(acac)_3$), 20 mg glucose, 40 mg hexadecyltrimethylammonium bromide (CTAB), and 5 mL oleylamine in a 20-mL glass vial and cap it (without purging with inert gas). Then, sonicate the mixture for 2 h to ensure uniform dispersion. Subsequently, the vial was placed in an oil bath at 200 °C and reacted for 5 h without stirring. After the reaction is completed, cool the solution to room temperature, wash with a cyclohexane and ethanol solvent (in a 9:1 volume ratio, and centrifuge at 9000 rpm for 10 min to obtain the $Pt_{58}Fe_{42}$ catalyst. The synthesis procedures for $Pt_{67}Fe_{33}$ and $Pt_{76}Fe_{24}$ are similar to that of $Pt_{58}Fe_{42}$, except for the amount of $Fe(acac)_3$. Specifically, 3 and 2.8 mg of $Fe(acac)_3$ were used for the synthesis of $Pt_{67}Fe_{33}$ and $Pt_{76}Fe_{24}$, respectively.

2.3 Preparation of Pt/C and PtFe/C

The PtFe (80 mg) obtained is dispersed in 60 mL of cyclohexane, followed by uniform mixing with 20 mg of XC72R carbon and continuous sonication for approximately 60 min. Following centrifugation, the solid product is isolated and subsequently washed with a cyclohexane/ethanol mixed solution (9:1, v/v). Furthermore, the solid product is then stirred overnight in acetic acid to remove surface residues. The PtFe/C catalyst was collected by centrifugation, with a measured PtFe loading of 80 wt%. Pt/C was synthesized following an identical procedure.

2.4 Characterizations

The X-ray diffraction (XRD) patterns of Pt and PtFe were obtained using a Rigaku D/max-2400 X-ray powder diffractometer, with Cu Kα ($\lambda = 1.5406$ nm) as the X-ray source. The morphologies of initial, discharged, and charged Pt and PtFe electrode were analyzed using high-resolution transmission electron microscopy (HR-TEM, Tecani-G2 T20), scanning electron microscopy (SEM, Thermo Fisher Quattro S system), X-ray photoelectron spectroscopy (XPS, Thermo Fisher ESCALAB XI+), Fourier transform infrared spectroscopy (FTIR, PerkinElmer Spectrum II FTIR Spectrometer), Raman (WITec alpha 300 Raman System), nuclear magnetic resonance (NMR, Bruker), and UV–vis spectra (Hitachi UH4150). Before conducting ex situ characterization, the Pt- and PtFe-based batteries are transferred to a glovebox (with O_2 and H_2O levels below 0.1 ppm) and disassembled. The PtFe and Pt electrodes are thoroughly rinsed with dimethyl sulfoxide to eliminate electrolyte and lithium salts. To avoid contamination, the PtFe and Pt electrodes should be securely sealed with Parafilm. To ensure accurate ex situ results, the PtFe and Pt electrodes are removed from the glovebox 5 min before testing.

2.5 Battery Assembly and Performances

To prepare PtFe electrodes, PVDF (10 wt%) was dispersed in NMP at 60 °C for 20 min. Subsequently, PtFe/C (90 wt%) was incorporated into the PVDF solution, followed by continuous magnetic stirring for 8 h to ensure a uniform mixture. Subsequently, the catalyst slurry was drop cast onto carbon paper substrates (0.21 mm thick, 10 mm diameter) and vacuum-dried at 60 °C for 24 h to fabricate the Pt/C (or PtFe/C) electrodes. The PtFe/C electrode has a surface area of 0.75 cm^2, with a loading mass of 3 to 4 mg cm^{-2} for PtFe/C or Pt. The assembly of coin cells (2032, 13 holes) was assembled in a glove box (with H_2O and O_2 concentration below 0.1 ppm). The coin cell includes FePt/C (Pt/C) cathode, a Li anode, separator, and electrolytes (10 µL, 1 M lithium trifluoromethanesulfonate in tetraethylene glycol dimethyl ether). The lithium anode was prepared before the assembly of the battery. Before testing, the coin cell will be placed in a specific container (with dry O_2 content above 99.99% at 1.0 atm.) and maintained at a constant temperature of 25 °C for 24 h in a constant-temperature chamber. The assembled coin cells (including PtFe/C or Pt/C) were analyzed by the NEWARE battery testing system to obtain full and limited discharge–charge curves. The cyclic voltammetry (CVs) was analyzed by an electrochemical workstation (CHI760e) from 2.0 to 4.5 V at a scan rate of 0.3 mV s^{-1}. EIS measurements were also carried out using the CHI760e electrochemical workstation, applying an amplitude voltage of 10 mV and a frequency range from 10^5 to 0.1 Hz.

2.6 Density Functional Theory Calculations

All density functional theory (DFT) calculations were performed using the Vienna Ab initio Simulation Package

(VASP). The Perdew–Burke–Ernzerhof generalized gradient approximation (PBE-GGA) was employed to describe exchange–correlation effects in all calculations. The interactions between ionic cores and valence electrons were modeled with the Projector Augmented-Wave (PAW) pseudopotential method. We set the plane-wave energy cutoff to 450 eV and relaxed all structures until the maximum Hellmann–Feynman forces fell below -0.02 eV Å^{-1}, and consecutive energy differences were less than 10^{-5} eV. Dispersion interactions between all atoms in the adsorption systems were accounted for using Grimme's DFT-D3 correction scheme. The lattice parameters used in the DFT calculations for the PtFe alloy were determined as follows. Based on the cubic unit cell of pure Pt, which aligns with the catalyst's XRD peak positions, we constructed a 100-atom supercell. In this supercell, Pt atoms were randomly replaced with Fe atoms to generate alloy models with compositions spanning $\mathrm{Pt_{58}Fe_{24}}$, $\mathrm{Pt_{67}Fe_{33}}$ and $\mathrm{Pt_{76}Fe_{24}}$. The atomic positions of each model were then optimized while keeping the experimental lattice constants fixed. The *d*-band center (ε_{d}) was calculated as the first moment of the projected *d*-orbital density of states (PDOS) of the surface Pt/Fe atoms, using the formula $\varepsilon_{\mathrm{d}} = \int E \times D(E)\mathrm{d}E \Big/ D(E)\mathrm{d}E$, where $D(E)$ is the DOS of *d*-band suborbital. The *d*-electron numbers were obtained by integrating the occupied part of the corresponding *d*-suborbital PDOS below Femi energy.

3 Results and Discussion

3.1 Synthesis and Characterization of PtFe Nanowires

The fabrication of PtFe nanowires is conducted using a typical wet chemical method. The obtained PtFe nanowires exhibit a zigzag-like morphology, with an average width of 10–20 nm (Fig. 1a, b). The XRD results demonstrate that the main peaks at 40.35°, 47.19°, 68.71°, 82.50°, and 86.71° are attributed to the (111), (200), (220), (311), and (222) planes of PtFe nanowires (Fig. 1c). It is worth noting that the peak intensity of the (111) facet of PtFe is stronger than that of the (200) and (220) facets. The results indicate that the (111) facet of $\mathrm{Pt_{58}Fe_{42}}$ exhibits a lower surface energy (4.68 J m^{-2}) compared to both the (200) facet (5.29 J m^{-2}) and the (220) facet (4.74 J m^{-2}). Consequently, the (111) facet of $\mathrm{Pt_{58}Fe_{42}}$ demonstrates superior thermodynamic stability (Fig. S1, Tables S1–S3). Due to the smaller atomic radius of Fe than that of Pt, the diffraction peaks of PtFe shift to higher angles of 2θ compared to those of pure Pt. The lattice spacing of 0.136, 0.19, and 0.221 nm corresponds to the (022), (200), and (111) crystal planes of PtFe nanowires, respectively (Fig. 1d). The Fourier transform (FFT) of the selected area in Fig. 1d shows different facets along the [011] zone axis (Fig. 1e), which is in accordance with the XRD results. The energy-dispersive X-ray spectroscopy (EDS) mapping reveals a homogeneous distribution of Pt and Fe within a single PtFe nanowire, with a molar ratio of Pt to Fe at 58:42 (Fig. 1f, g). In addition, two other PtFe electrocatalysts with different Pt ratios ($\mathrm{Pt_{67}Fe_{33}}$ and $\mathrm{Pt_{76}Fe_{24}}$) were also successfully synthesized (Figs. S2 and S3).

3.2 Electrocatalytic Performances of PtFe Nanowires

Pure Pt and the PtFe nanowires are further employed as cathode electrocatalysts in Li–$\mathrm{O_2}$ batteries. Under a discharge capacity limitation of 1 mAh cm^{-2} at 0.1 mA cm^{-2} with 3 mg cm^{-2} mass loading, $\mathrm{Pt_{58}Fe_{42}}$ demonstrates the lowest charge overpotential (0.24 V) and highest energy efficiency (84%) (Fig. 2a), significantly outperforming pure Pt (0.69 V), $\mathrm{Pt_{67}Fe_{33}}$ (0.41 V), and $\mathrm{Pt_{76}Fe_{24}}$ (0.92 V) (Fig. S4). In the subsequent study, the best-performing $\mathrm{Pt_{58}Fe_{42}}$ was selected for comparison with pure Pt. Since the discharge products of $\mathrm{Li_2O_2}$ primarily form on the catalyst surface during discharge, the capacity is largely determined by the catalyst's specific surface area, which governs the deposition capacity of $\mathrm{Li_2O_2}$. Owing to its high specific surface area of 261 m^2 g^{-1}, $\mathrm{Pt_{58}Fe_{42}}$ consequently delivers a full-discharge areal capacity of 11.59 mAh cm^2 and an energy density of 1200 Wh kg^{-1} (including the total mass of the cathode, electrolyte, binder, and $\mathrm{Li_2O_2}$; calculation details are provided in Table S4) at a current density of 0.4 mA cm^{-2} (Fig. 2b). These values exceed those of Pt/C, which exhibits a lower specific surface area of 84 m^2 g^{-1} (Fig. S5) and achieves 981 Wh kg^{-1} and 8.72 mAh cm^{-2}. Moreover, $\mathrm{Pt_{58}Fe_{42}}$ demonstrates a charge overpotential of 0.67 V, much lower than the 1.38 V of Pt (Fig. 2b). The cyclic voltammetry (CV) spectra further demonstrate that $\mathrm{Pt_{58}Fe_{42}}$ shows a higher exchange current density of 19.63 μA cm^{-2} than that of the pure Pt (11.96 μA cm^{-2}), confirming the exceptional OER kinetics of $\mathrm{Pt_{58}Fe_{42}}$ (Fig. 2c). Furthermore, under capacity-limited cycling (1 mAh cm^{-2}), Pt could only endure cycling for

https://doi.org/10.1007/s40820-026-02085-z

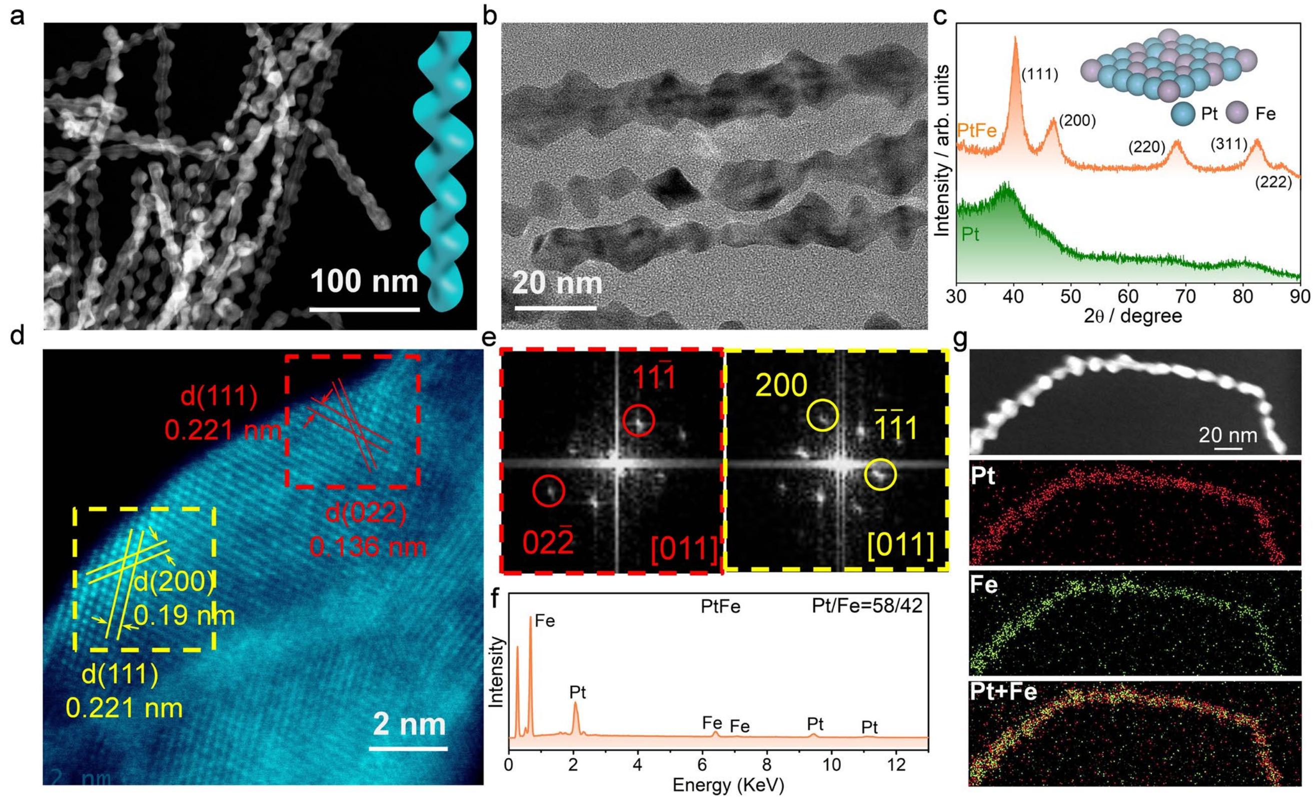

Fig. 1 **a, b** TEM images of PtFe nanowires. **c** XRD patterns of Pt and PtFe nanowires. **d** HAADF-STEM image of PtFe nanowires. **e** FFT patterns of the dashed squares in corresponding colors in (d) for PtFe nanowires. **f** EDX spectra of PtFe nanowires. **g** EDS mapping of Pt and Fe elements based on a single PtFe nanowire

100 cycles due to severe charge polarizations (Fig. 2d). In contrast, $Pt_{58}Fe_{42}$ maintained stable charge–discharge characteristics even after 250 cycles (1000 h) at 0.5 mA cm^{-2}, showing no notable performance degradation (Fig. 2d). Even at a capacity of 1000 mAh g^{-1} (3 mAh cm^{-2}), the $Pt_{58}Fe_{42}$ catalyst can still maintain stable cycling for 200 cycles at a current density of 0.75 A g^{-1} (Fig. 2e). The combination of low charge overpotential and long cycle stability of $Pt_{58}Fe_{42}$ electrocatalysts surpasses the results of the majority of noble metal-based cathode electrocatalysts (Fig. 2f and Table S5).

3.3 Reversibility Analysis of $Pt_{58}Fe_{42}$ Nanowires

To reveal the reversibility of $Pt_{58}Fe_{42}$ electrocatalysts, the morphologies of the discharged $Pt_{58}Fe_{42}$ and Pt are analyzed using SEM. When discharged at 1 mAh cm^{-2}, the discharged $Pt_{58}Fe_{42}$ cathode exhibits a disk-shaped morphology with a diameter of 2–3 μm (Fig. 3a), which have been identified as Li_2O_2 (Figs. S6–S8). Compared to $Pt_{58}Fe_{42}$, the vast majority of discharge products on the Pt electrode are disk-shaped (4 μm in diameter), whereas a negligible portion exhibits a distinct sphere morphology (Figs. S9–S11). For $Pt_{58}Fe_{42}$, the low surface energy (0.29 eV Å^{-2}) of its (111) facet facilitates the disproportionation of the intermediate LiO_2 in solution, resulting in the formation of typical disk-shaped discharge products via the solution growth mechanism. In contrast, for the Pt catalyst, the relatively high surface energy of (111) facet (0.38 eV Å^{-2} in Fig. S12 and Table S6) promotes partial adsorption of intermediates on the surface, where they may undergo either reduction or disproportionation reactions. Consequently, a small number of spherical discharge products are observed on the Pt electrode, representing a morphology that lies between the thin films formed by the pure surface growth model and the disk structures produced via the dissolution pathway. The small disk-shaped Li_2O_2 indicates good interfacial contact with the $Pt_{58}Fe_{42}$ cathode, resulting in a significantly lower charge transfer resistance of 115.6 Ω compared to 811.2 Ω for larger-diameter Li_2O_2 on $Pt_{58}Fe_{42}$ (Fig. S13 and Table S7). The reversibility of

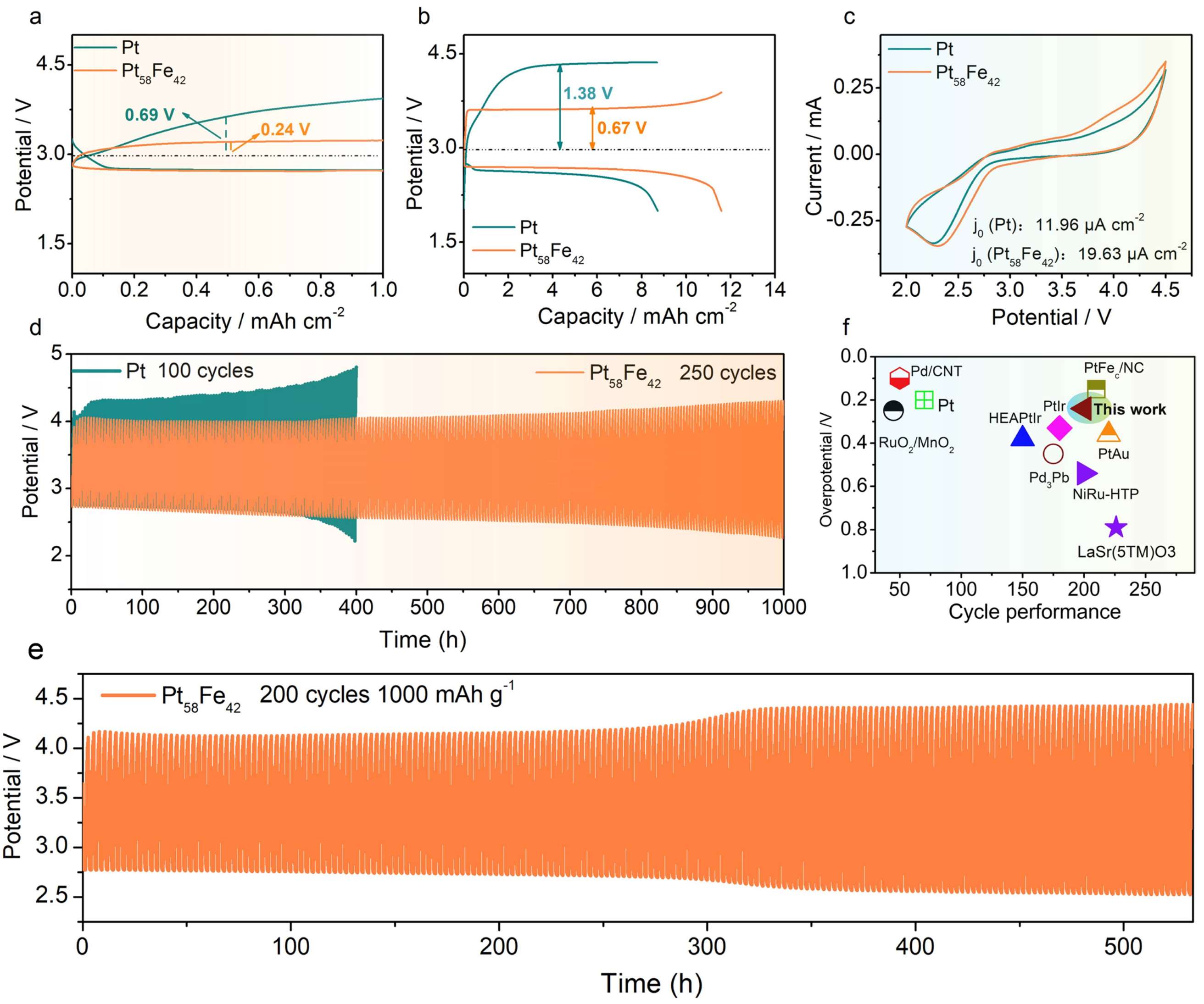

Fig. 2 **a** Discharge–charge curves of Pt and $Pt_{58}Fe_{42}$ electrocatalysts with a limited capacity of 1 mAh cm^{-2}. **b** Full discharge–charge profiles of Pt and $Pt_{58}Fe_{42}$ nanowire. **c** CVs curves for Pt and $Pt_{58}Fe_{42}$ electrocatalysts from 2.0 to 4.5 V. **d** Cycle performance of Pt and $Pt_{58}Fe_{42}$ electrocatalysts at 1 mAh cm^{-2} under a current density of 0.5 mA cm^{-2}. **e** Cycling stability performance of $Pt_{58}Fe_{42}$ at 1000 mAh g^{-1} and a current density of 0.75 A g^{-1}. **f** Examining the charge overpotentials and cycle stability of $Pt_{58}Fe_{42}$ nanowires with a variety of electrocatalysts, including RuO_2/MnO_2 [41], Pd/CNT [42], Pt [43], HEAPtIr [44], Pd_3Pb [45], PtIr [18], NiRu-HTP [46], $PtFe_c$/NC [47], PtAu [17], and $LaSr(5TM)O_3$ [48]

$Pt_{58}Fe_{42}$ and Pt is further investigated under charging and discharging conditions through SEM images, XRD patterns, Raman spectra, and XPS spectra. During the initial, the 1st discharged, the 1st charged, the 10th discharged, the 10th charged, the 20th discharged, and the 20th charged processes, Li_2O_2 can be reversibly formed and decomposed on the $Pt_{58}Fe_{42}$ cathodes (Fig. 3a–k). Due to the overlap of the O 1*s* signals of $Pt_{58}Fe_{42}$ and Pt with those of O 1*s* in Li_2CO_3 in the XPS spectra (Figs. S14 and S15), Li 1*s* and C 1*s* are employed for the analysis of discharge products and byproducts (Fig. S16). In addition, negligible valence variations for Pt and Fe can be detected after the 20th charge–discharge cycle (Figs. S17 and S18), with a uniform distribution of Pt and Fe elements even after the 20th recharge cycle (Fig. 3l, m). Conversely, the high charge polarization of Pt leads to the generation of significant byproducts (Li_2CO_3) after the initial charging process (Figs. S19 and S20). UV–Vis absorption spectra further confirmed that the

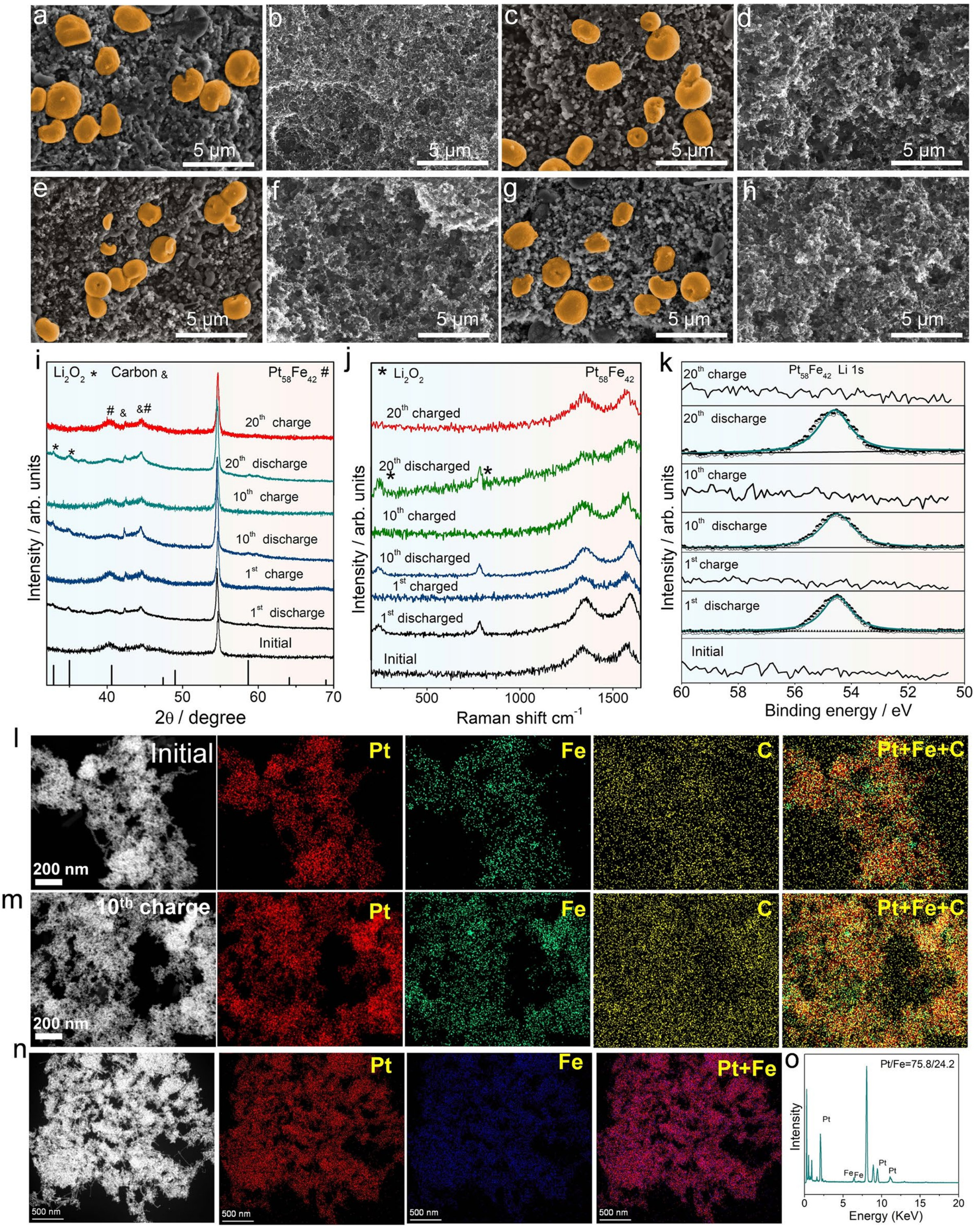

Fig. 3 **a–h** SEM images of 1st discharged (**a**), 1st charged (**b**), 5th discharged (**c**), 5th charged (**d**), 10th discharged (**e**), 10th charged (**f**), 20th discharged (**g**), 20th charged (**h**) cathode. **i–k** XRD patterns (**i**), Raman spectra (**j**) and XPS spectra (**k**) of $Pt_{58}Fe_{42}$ cathode at initial, 1st discharged and charged, 5th discharged and charged, 10th discharged and charged, and 20th discharged and charged state. **l, m** Elemental mapping of C, Pt, and Fe distribution for initial (l) and 10th charged (m) $Pt_{58}Fe_{42}$ cathode. **n** Elemental mapping of Pt, and Fe distribution for 200th charged $Pt_{58}Fe_{42}$ cathode. **o** EDX spectra of 200th charged $Pt_{58}Fe_{42}$ nanowires

lithium–oxygen battery based on $Pt_{58}Fe_{42}$ exhibits a higher Li_2O_2 formation efficiency (86%) and a lower residual Li_2O_2 ratio (12.5%) after the first discharge–charge cycle compared to Pt (Li_2O_2 formation efficiency: 80%; residual Li_2O_2: 37.5% in Fig. S21). When the discharge capacity is increased to 1000 mAh g^{-1} (3 mAh cm^{-2}), TEM images reveal a uniform distribution of Pt and Fe elements even after the 100th recharge cycle, demonstrating the cycling stability of the $Pt_{58}Fe_{42}$ catalyst (Fig. S22).

Furthermore, with a limited capacity of 1 mAh cm^{-2}, TEM characterization of the $Pt_{58}Fe_{42}$ catalyst after the 200th cycle indicates an increase in the Pt/Fe ratio from 58:42 to 75.8:24.2 (Fig. 3n, o). This change results in poor OER activity and high charge overpotentials, ultimately leading to the incomplete decomposition of Li_2O_2 during charging (Fig. S23) and a reduction in the battery's cycling stability.

3.4 Electron State Analysis of d_z^2 Frontier Orbital in $Pt_{58}Fe_{42}$ Nanowires

The Bader charge and differential charge densities are employed to analyze the OER catalytic activities of the $Pt_{58}Fe_{42}$ electrocatalysts. Because Pt is more electronegative than Fe, electron transfer occurs from Fe to Pt, resulting in a reduced valence band energy for Pt in $Pt_{58}Fe_{42}$ versus pure Pt (Fig. 4a), as confirmed by XPS measurements (Fig. S24). The lower valence of Pt in $Pt_{58}Fe_{42}$ is further supported by the differential charge density, showing that Pt exhibits a higher electron density compared to that of Pt in Pt (Fig. 4b, c). The electron localization function analysis reveals a higher degree of electron localization around Pt in PtFe compared to pure Pt, suggesting electron transfer from Fe to Pt (Fig. S25). Furthermore, Raman spectroscopy of CO adsorbed on Pt and PtFe surfaces indicates that on the PtFe alloy surface, CO preferentially a dsorbs at Pt sites with specific coordination environments. Relative to pure Pt, the *d*-electron density at these Pt sites increases due to the electronic effect of Fe (reflected by a lower apparent oxidation state), which enhances π-back-donation from the metal to CO. This weakens the C–O bond and results in a redshift of the C–O vibrational peak (Fig. 4d). Such lower valence band leads to a downward shift of the Pt 5*d* band center (−7.72 eV) compared to the − 7.18 eV of pure Pt from ultraviolet photoelectron spectroscopy (UPS) results (Fig. S26). Therefore, the transfer of electrons from Fe to Pt in $Pt_{58}Fe_{42}$ causes the *d*-band center of Fe to shift upward compared to that in pure Pt, while the *d*-band center of Pt shifts downward relative to pure Pt (Fig. S27). The downward shift of the Pt 5 *d*-band center in $Pt_{58}Fe_{42}$ indicates a change in the electron occupancy of Pt's five d-suborbitals. For the case of pure Pt, the number of electrons in its five suborbitals d_{yz}, d_{xz}, d_{xy}, $d_x^2{}_{-y}^2$, and d_z^2 is 1.80, 1.80, 1.76, 1.82, and 1.76, respectively (Fig. 4e). In $Pt_{58}Fe_{42}$, electron transfers from Fe to Pt involves Pt $d_{xz/yz/xy}$–Fe $d_{xz/yz/xy}$, Pt $d_x^2{}_{-y}^2$–Fe $d_x^2{}_{-y}^2$, and Pt d_z^2–Fe d_z^2 orbital interactions (Fig. 4f). The strength of orbital interaction between the Pt and Fe suborbitals primarily depends on the energy gap between their respective *d*-band centers. A smaller *d*-band center gap indicates stronger orbital coupling, which facilitates greater electron transfer from the Fe suborbital to the corresponding Pt suborbital. Due to the significantly lower *d*-band center gap between Pt d_z^2 and Fe d_z^2 (0.3 eV, Fig. 4g), compared to those of Fe d_{xz}–Pt d_{xz} (0.41 eV), Fe d_{yz}–Pt d_{yz} (0.45 eV), Fe d_{xy}–Pt d_{xy} (0.37 eV), and Pt $d_x^2{}_{-y}^2$–Fe $d_x^2{}_{-y}^2$ (0.40 eV), the Pt d_z^2–Fe d_z^2 coupling is the strongest in Pt–Fe interaction (Fig. 4h). Therefore, the electron transfer between Pt and Fe mainly concentrates on Pt d_z^2–Fe d_z^2 (0.16 e^-), in contrast to those of Fe d_{xz}–Pt d_{xz} (0.04 e^-), and Fe d_{yz}–Pt d_{yz} (0.01 e^-), Fe d_{xy}–Pt d_{xy} (0.07 e^-), Pt $d_x^2{}_{-y}^2$–Fe $d_x^2{}_{-y}^2$ (0.03 e^-). Therefore, the *d*–*d*-orbital coupling between Pt and Fe in Pt58Fe42 leads to an increase in the electron occupancy of the Pt d_z^2 orbital to 1.92, compared to 1.76 in pure Pt. Compared to pure Pt, the additional electron in the Pt d_z^2 frontier orbital in $Pt_{58}Fe_{42}$ will participate in the hybridization interaction with fully occupied 5σ interaction of LiO_2.

3.5 Frontier Orbital Interaction between $Pt_{58}Fe_{42}$ and LiO_2

During the interaction between Pt and LiO_2, the d_z^2 and d_{xz}/d_{yz} orbitals of Pt interact with the 5σ and 2π orbitals of LiO_2, respectively, leading to the formation of new σ and π bonds. Given that σ bonds are intrinsically stronger than π bonds, modulating the σ-bond interaction (involving the Pt d_z^2 orbital) is more effective in reducing the charge overpotential than tuning the π-bond interaction. Therefore, the d_z^2 orbital of Pt and the 5σ orbital of LiO_2 are considered to be the frontier orbitals. It should be noted that the modulation of the d_z^2 electron occupancy in Pt within $Pt_{58}Fe_{42}$

primarily governs the charging overpotential and thereby the battery's energy efficiency, while contributing minimally to the discharge capacity. Due to the distinction in the electron number of the d_{z}^{2} orbitals in Pt and $Pt_{58}Fe_{42}$ cathodes, the orbital interaction between the Pt d_{z}^{2} frontier orbital in Pt (or $Pt_{58}Fe_{42}$) and the 5σ frontier orbital of LiO_2 is further analyzed, which is the key factor determining the OER kinetics. The frontier orbital interaction between the d_{z}^{2} orbital of Pt and the 5σ orbital of LiO_2 will form a bonding orbital of d_{z}^{2}-5σ and an antibonding orbital of d_{z}^{2}-5σ* (Fig. 5a, b). The interaction strength between the Pt-based catalyst (Pt or $Pt_{58}Fe_{42}$) and LiO_2 depends on the bond order, which is calculated as (A-B)/2, where A and B represent the electron number in the bonding and antibonding levels, respectively. As shown in Fig. 5c, d, the higher electron count in the d_{z}^{2} orbital of Pt in $Pt_{58}Fe_{42}$ leads to more electron occupation in the antibonding level of d_{z}^{2}-5σ*, resulting in a lower bond order (0.02) between $Pt_{58}Fe_{42}$ and the adsorbed LiO_2, compared to that of pure Pt (0.12). Thermodynamically, this favors the desorption and decomposition of LiO_2, facilitating a rapid OER on the $Pt_{58}Fe_{42}$ surface. In the $Pt_{58}Fe_{42}$ catalyst, Pt serves as the primary catalytic site. The main role of Fe is to modulate the electronic state of Pt, thereby fine-tuning the adsorption of reaction intermediates and enhancing the overall catalytic performance. This is further corroborated by theoretical calculations: The Gibbs free energy profile reveals that the charging overpotential for Li_2O_2 decomposition on a pure Fe catalyst is as high as 2.0 V. This result explicitly excludes Fe as the active catalytic center (Fig. S28). The weaker adsorption strength between LiO_2 and $Pt_{58}Fe_{42}$ (−5.29 eV) compared to Pt (−5.56 eV) is further evidenced by differential charge density and Bader charge analyses, where a lower electron transfer of 0.74 e^- from $Pt_{58}Fe_{42}$ to LiO_2 is found, compared to the transfer of 1.03 e^- from Pt (Fig. 5e, f). Moreover, UV–Vis spectra suggest that, in the presence of the $Pt_{58}Fe_{42}$ catalyst, the adsorption of O_2^- is higher in the solution of KO_2 + dimethyl sulfoxide (DMSO), further confirming that $Pt_{58}Fe_{42}$ exhibits a weaker adsorption strength toward O_2^- (Fig. 5g). In addition, compared to Pt, $Pt_{58}Fe_{42}$ exhibits weaker adsorption not only toward LiO_2 (as previously noted) but also toward O_2, Li_2O_2, and Li_4O_4, demonstrating a similar trend (Figs. 5h–j and S29). The weaker adsorption of LiO_2 by $Pt_{58}Fe_{42}$ results in a lower charge overpotential, as evidenced by Gibbs free energy calculations. During the charging process, the charge overpotential $\eta = U_c - U_0$, where U_c and U_0 represent the charge overpotential and equilibrium potential. In the rate-determining step (Fig. 5l), LiO_2 decomposes into O_2 and Li^+. The weak orbital interaction between LiO_2 and $Pt_{58}Fe_{42}$ results in a lower charge energy barrier of 0.53 eV (Fig. 5l) compared to that of Pt (0.61 eV in Fig. 5k). This finding is in line with the activation energy results obtained from electrochemical impedance spectra (Figs. 5m and S30–S33). As a result, all the aforementioned results suggest that the frontier orbital interactions between the Pt d_{z}^{2} orbital in PtFe and the 5σ orbital of LiO_2 can effectively enhance the OER kinetics of Li–O_2 batteries.

We further calculated DOSs and Gibbs free energy profiles for $Pt_{67}Fe_{33}$ and $Pt_{76}Fe_{24}$ to elucidate why the $Pt_{58}Fe_{42}$ catalyst exhibits superior OER performance. The results indicate that as the Pt content increases (from $Pt_{58}Fe_{42}$ to $Pt_{67}Fe_{33}$ and $Pt_{76}Fe_{24}$), the electron population in the Pt 5 d_{z}^{2} orbital gradually decreases, with values of 1.92 for $Pt_{58}Fe_{42}$, 1.85 for $Pt_{67}Fe_{33}$, and 1.80 for $Pt_{76}Fe_{24}$ (Fig. S34). This progressive depletion in the Pt 5 d_{z}^{2} orbital leads to a corresponding increase in the adsorption strength of the LiO_2 intermediate, as evidenced by the more negative adsorption energies: −5.29 eV for $Pt_{58}Fe_{42}$, −6.17 eV for $Pt_{67}Fe_{33}$, and −6.41 eV for $Pt_{76}Fe_{24}$ (Fig. S35). Moreover, the weakening interaction with LiO_2 across the series from $Pt_{58}Fe_{42}$ to $Pt_{76}Fe_{24}$ corresponds to a decline in OER activity, which is reflected in the increasing overpotentials derived from the Gibbs free energy diagrams: 0.53 V for $Pt_{58}Fe_{42}$, 3.08 V for $Pt_{67}Fe_{33}$, and 3.41 V for $Pt_{76}Fe_{24}$ (Figs. S36 and S37).

To further establish the universality of Pt d_{z}^{2} orbital electrons as a descriptor for OER activity, we supplemented our study with other Pt-based alloy catalysts. Using PtCo ($Pt_{82}Co_{18}$, $Pt_{70}Co_{30}$, $Pt_{64}Co_{36}$) and PtCu ($Pt_{78}Cu_{22}$, $Pt_{68}Cu_{32}$, $Pt_{59}Cu_{41}$) as typical examples, we verified the correlation between Pt d_{z}^{2} orbital electrons and OER performance. The results consistently show that for both PtCo and PtCu systems, OER activity gradually decreases with a reduction in the number of Pt d_{z}^{2} orbital electrons (Figs. S38–S43). This demonstrates that the identified relationship is not limited to PtFe but extends to other Pt-based alloys, confirming that Pt d_{z}^{2} orbital electrons can serve as a universal descriptor for OER activity across Pt-based catalysts.

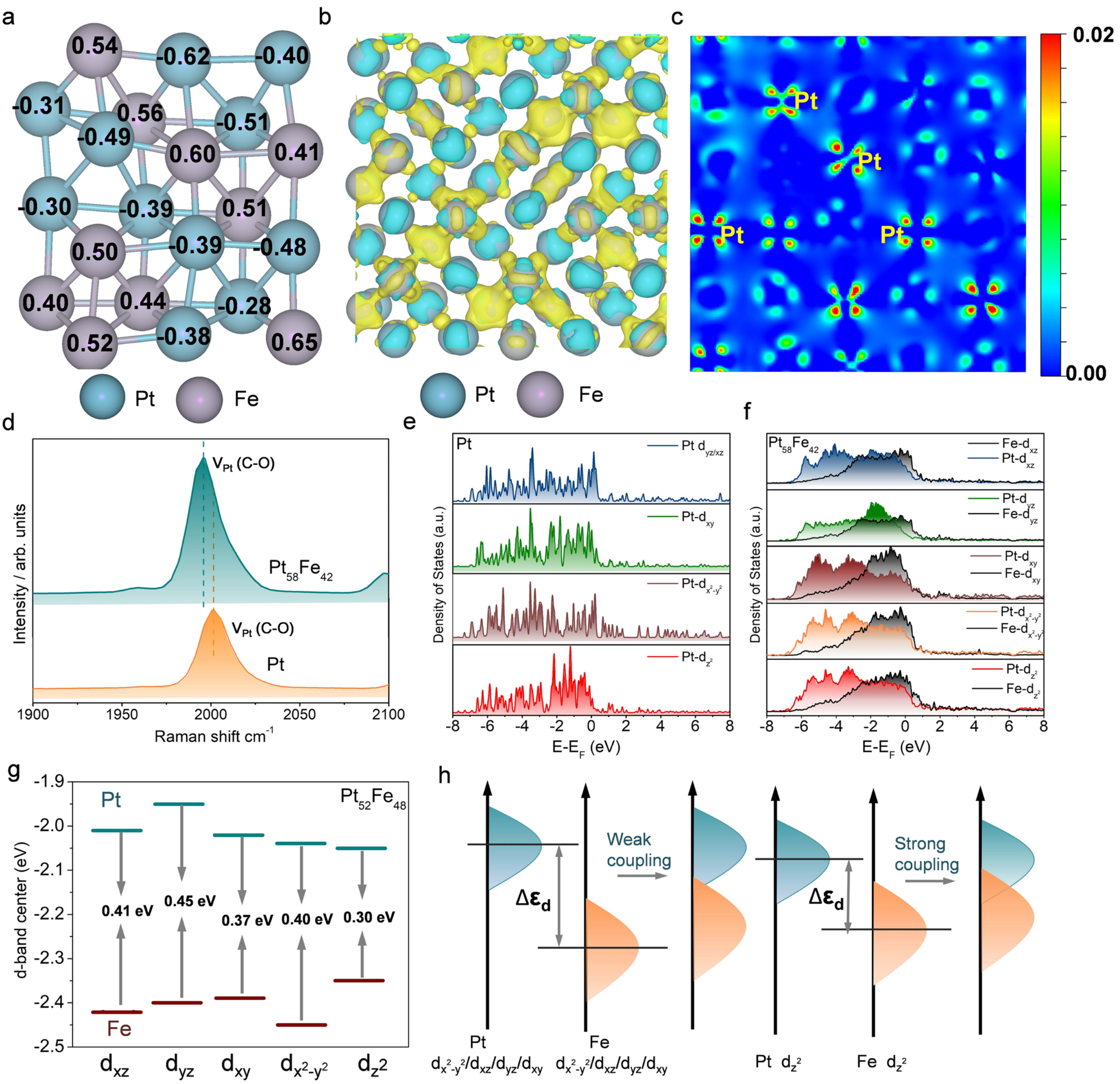

Fig. 4 **a** Bader charge results of $Pt_{58}Fe_{42}$ nanowires. **b c** The differential charge density (**b**) and two-dimensional charge density (**c**) for $Pt_{58}Fe_{42}$ nanowires. **d** Raman spectra of Pt and $Pt_{58}Fe_{42}$ under a CO atmosphere. **e f** DOSs of Pt 5d orbital for $d_{yz/xz}$, d_{xy}, $d_x^2-_y^2$ and d_z^2 in Pt (**e**) and $Pt_{58}Fe_{42}$ (**f**). **g** The d-band center gap of Pt d_{xy}-Fe d_{xy}, Pt d_{xz}-Fe d_{xz}, Pt d_{yz}-Fe d_{yz},Pt $d_x^2-_y^2$ -Fe $dx2x2_x^2-_y^2$, and Pt d_z^2-Fe d_z^2 in $Pt_{58}Fe_{42}$. **h** The influence of d-band center gap on the coupling strength between Pt and Fe in $Pt_{58}Fe_{42}$

4 Conclusions

In conclusion, we have constructed a Pt-based model catalyst to investigate the relationship between the number of Pt $d_z{}^2$ frontier orbital electrons and OER activity for Li–O_2 batteries. Subsequently, when the $d_z{}^2$ frontier orbital of Pt in the PtFe catalyst interacts with the 5σ frontier orbital of LiO_2, the excess electrons in the Pt $d_z{}^2$ orbital occupy the antibonding orbital, thereby weakening the interaction with LiO_2 and ultimately enhancing the OER catalytic activity. This work

https://doi.org/10.1007/s40820-026-02085-z

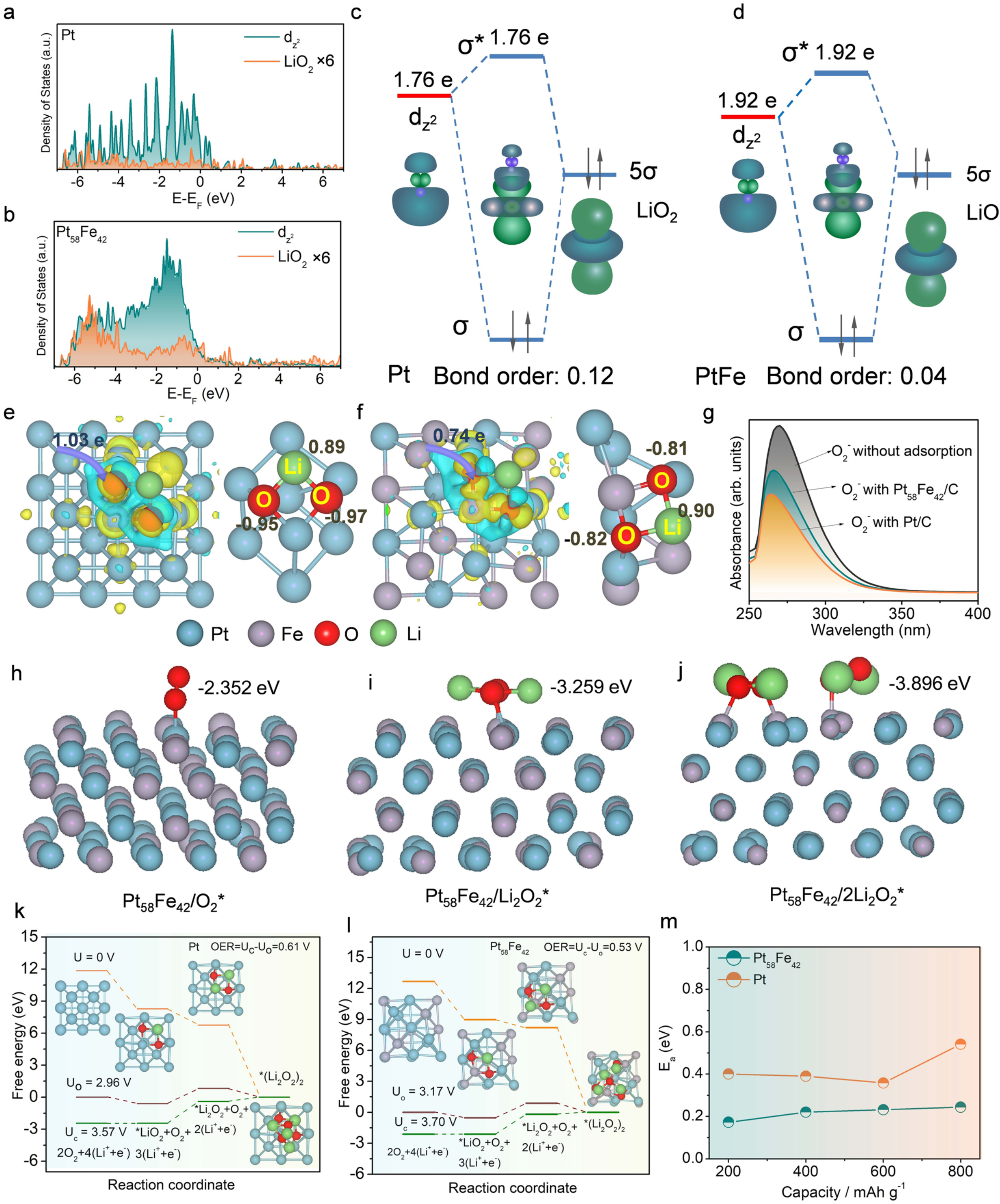

Fig. 5 **a, b** DOSs curves for the orbital hybridization between Pt 5d and adsorbed LiO_2 for Pt (**a**) and $Pt_{58}Fe_{42}$ (**b**). **c, d** Orbital hybridization between LiO_2 and Pt (**d**) or $Pt_{58}Fe_{42}$. **e, f** Differential charge density on Pt/LiO_2 (**e**) and $Pt_{58}Fe_{42}$-LiO_2 (**f**). **g** UV–Vis spectra for adsorbed Pt and $Pt_{58}Fe_{42}$ electrocatalysts with KO_2/DMSO solution. **k, l** Gibbs free energy profiles of Pt and $Pt_{58}Fe_{42}$ at various potentials. **h–j** Optimized structures of $Pt_{58}Fe_{42}/O_2^*$, $Pt_{58}Fe_{42}/Li_2O_2^*$ and $Pt_{58}Fe_{42}/2Li_2O_2^*$. **m** Activating energy for the charge process at different capacities by using Pt and $Pt_{58}Fe_{42}$ nanowires

established a correlation between the number of electrons in the d_z^2 frontier orbital and OER activity, suggesting that the electron number in the d_z^2 frontier orbital can serve as a descriptor for OER activity.

Acknowledgements This work was financially supported by the National Natural Science Foundation of China/RGC Joint Research Scheme (N_CityU156/25), Green Tech Fund (GTF202220105), Guangdong Basic and Applied Basic Research Foundation (2024A1515011008), the Research Grants Council of the Hong Kong Special Administrative Region, China (Project No. PDFS2425-1S03), City University of Hong Kong (CityU9020002, CityU9680374), National Natural Science Foundation of China (52561160149), Natural Science Foundation of Shandong Province (ZR2024QB045), and the Shenzhen Research Institute of City University of Hong Kong.

Author Contributions GH supervised the project. YZ, KY, TZ, and DF conducted the catalyst fabrication and finished the performance test. JL conducted the DFT calculations. YZ, AZ, DL, YL, YL, KL, HY, HC, and KL analyzed the data. YZ wrote the manuscript. CL, HC and YY commented on the manuscript. GH revised the manuscript.

Declarations

Conflict of Interest The authors declare no interest conflict. They have no known competing financial interests or personal relationships that could have appeared to influence the work reported in this paper.

Supplementary Information The online version contains supplementary material available at https://doi.org/10.1007/s40820-026-02085-z.

References

1. H. Yu, G. Zhang, D. Zhang, R. Yang, X. Li et al., Homogeneous in-plane lattice strain enabling d-band center modulation and efficient d–π interaction for an $Ag_2Mo_2O_7$ cathode catalyst with ultralong cycle life in Li–O_2 batteries. Adv. Energy Mater. **14**(36), 2401509 (2024). https://doi.org/10.1002/aenm.202401509
2. Y. Zhou, S. Guo, Recent advances in cathode catalyst architecture for lithium–oxygen batteries. eScience **3**(4), 100123 (2023). https://doi.org/10.1016/j.esci.2023.100123
3. D. Du, Z. Zhu, K.-Y. Chan, F. Li, J. Chen, Photoelectrochemistry of oxygen in rechargeable Li–O_2 batteries. Chem. Soc. Rev. **51**(6), 1846–1860 (2022). https://doi.org/10.1039/d1cs00877c
4. Z. Jiang, B. Wen, Y. Huang, Y. Guo, Y. Wang et al., New reaction pathway of superoxide disproportionation induced by a soluble catalyst in Li–O_2 batteries. Angew. Chem. Int. Ed. **63**(1), e202315314 (2024). https://doi.org/10.1002/anie.202315314
5. T. Lu, Y. Qian, K. Liu, C. Wu, X. Li et al., Recent progress of electrolyte materials for solid-state lithium–oxygen (air) batteries. Adv. Energy Mater. **14**(26), 2400766 (2024). https://doi.org/10.1002/aenm.202400766
6. S. Xing, Z. Zhang, Y. Dou, M. Li, J. Wu et al., An efficient multifunctional soluble catalyst for Li–O_2 batteries. CCS Chem. **6**(7), 1810–1820 (2024). https://doi.org/10.31635/ccschem.023.202303320
7. Z. Li, S. Weng, X. Wu, C. Song, X. Yu et al., Tuning solid electrolyte interface against oxygen/superoxide-derived attack on Li-metal anode in Li–O_2 battery. Next Energy **1**(3), 100036 (2023). https://doi.org/10.1016/j.nxener.2023.100036
8. Y. Huang, H. Fang, J. Geng, T. Zhang, W. Hu et al., Anionic solvation transition at low temperatures for reversible anodes in lithium–oxygen batteries. J. Am. Chem. Soc. **146**(38), 26516–26524 (2024). https://doi.org/10.1021/jacs.4c10187
9. Y. Huang, J. Geng, Z. Jiang, M. Ren, B. Wen et al., Solvation structure with enhanced anionic coordination for stable anodes in lithium–oxygen batteries. Angew. Chem. Int. Ed. **62**(30), e202306236 (2023). https://doi.org/10.1002/anie.202306236
10. M. Li, J. Wu, Z. You, Z. Dai, Y. Gu et al., Crown ether electrolyte induced Li_2O_2 amorphization for low polarization and long lifespan Li–O_2 batteries. Angew. Chem. Int. Ed. **63**(27), e202403521 (2024). https://doi.org/10.1002/anie.202403521
11. S.-L. Tian, L.-N. Song, L.-M. Chang, W.-Q. Liu, H.-F. Wang et al., A force-assisted Li−O_2 battery based on piezoelectric catalysis and band bending of MoS_2/Pd cathode. Adv. Energy Mater. **14**(9), 2303215 (2024). https://doi.org/10.1002/aenm.202303215
12. B. Kim, M.-C. Sung, G.-H. Lee, B. Hwang, S. Seo et al., Aligned ion conduction pathway of polyrotaxane-based electrolyte with dispersed hydrophobic chains for solid-state lithium–oxygen batteries. Nano-Micro Lett. **17**(1), 31 (2024). https://doi.org/10.1007/s40820-024-01535-w
13. E.J. Askins, M.R. Zoric, M. Li, R. Amine, K. Amine et al., Triarylmethyl cation redox mediators enhance Li–O_2 battery discharge capacities. Nat. Chem. **15**(9), 1247–1254 (2023). https://doi.org/10.1038/s41557-023-01268-0
14. Z. Sun, X. Lin, W. Dou, Y. Tan, A. Hu et al., Redox mediator with the function of intramolecularly disproportionating superoxide intermediate enabled high-performance Li–O_2

batteries. Adv. Energy Mater. **12**(12), 2270050 (2022). https://doi.org/10.1002/aenm.202270050

15. Y. Dou, Z. Xie, Y. Wei, Z. Peng, Z. Zhou, Redox mediators for high-performance lithium–oxygen batteries. Natl. Sci. Rev. **9**(4), nwac040 (2022). https://doi.org/10.1093/nsr/nwac040
16. Y. He, L. Ding, J. Cheng, S. Mei, X. Xie et al., A "trinity" design of Li–O_2 battery engaging the slow-release capsule of redox mediators. Adv. Mater. **35**(49), 2308134 (2023). https://doi.org/10.1002/adma.202308134
17. Y. Zhou, Q. Gu, K. Yin, Y. Li, L. Tao et al., Engineering e(g) orbital occupancy of Pt with Au alloying enables reversible Li–O_2 batteries. Angew. Chem. Int. Ed. **61**(26), e202201416 (2022). https://doi.org/10.1002/anie.202201416
18. Y. Zhou, K. Yin, Q. Gu, L. Tao, Y. Li et al., Lewis-acidic PtIr multipods enable high-performance Li–O_2 batteries. Angew. Chem. Int. Ed. **60**(51), 26592–26598 (2021). https://doi.org/10.1002/anie.202114067
19. Y. Zhou, G. Hong, W. Zhang, Nanoengineering of cathode catalysts for Li–O_2 batteries. ACS Nano **18**(26), 16489–16504 (2024). https://doi.org/10.1021/acsnano.4c04420
20. P. Zhang, X. Hui, Y. Nie, R. Wang, C. Wang et al., New conceptual catalyst on spatial high-entropy alloy heterostructures for high-performance Li–O_2 batteries. Small **19**(15), 2206742 (2023). https://doi.org/10.1002/smll.202206742
21. W.-B. Jung, H. Park, J.-S. Jang, D.Y. Kim, D.W. Kim et al., Polyelemental nanoparticles as catalysts for a Li–O_2 battery. ACS Nano **15**(3), 4235–4244 (2021). https://doi.org/10.1021/acsnano.0c06528
22. D. Cao, L. Zheng, Q. Li, J. Zhang, Y. Dong et al., Crystal phase-controlled modulation of binary transition metal oxides for highly reversible Li–O_2 batteries. Nano Lett. **21**(12), 5225–5232 (2021). https://doi.org/10.1021/acs.nanolett.1c01276
23. Z. Sun, X. Cao, M. Tian, K. Zeng, Y. Jiang et al., Synergized multimetal oxides with amorphous/crystalline heterostructure as efficient electrocatalysts for lithium–oxygen batteries. Adv. Energy Mater. **11**(22), 2100110 (2021). https://doi.org/10.1002/aenm.202100110
24. Y. Xia, L. Wang, G. Gao, T. Mao, Z. Wang et al., Constructed Mott-Schottky heterostructure catalyst to trigger interface disturbance and manipulate redox kinetics in Li–O_2 battery. Nano-Micro Lett. **16**(1), 258 (2024). https://doi.org/10.1007/s40820-024-01476-4
25. Q. Xia, L. Zhao, Z. Zhang, J. Wang, D. Li et al., $MnCo_2S_4$-$CoS_{1.097}$ heterostructure nanotubes as high efficiency cathode catalysts for stable and long-life lithium–oxygen batteries under high current conditions. Adv. Sci. **8**(22), 2103302 (2021). https://doi.org/10.1002/advs.202103302
26. Z. Zhou, L. Zhao, J. Wang, Y. Zhang, Y. Li et al., Optimizing eg orbital occupancy of transition metal sulfides by building internal electric fields to adjust the adsorption of oxygenated intermediates for Li–O_2 batteries. Small **19**(41), 2302598 (2023). https://doi.org/10.1002/smll.202302598
27. Y. Dou, Z. Liu, L. Zhao, J. Zhang, F. Meng et al., Constructing double heterojunctions on 1T/2H-MoS_2@Co_3S_4 electrocatalysts for regulating Li_2O_2 formation in lithium–oxygen batteries. Nano-Micro Lett. **18**(1), 51 (2025). https://doi.org/10.1007/s40820-025-01895-x
28. E. Zhang, A. Dong, K. Yin, C. Ye, Y. Zhou et al., Electron localization in rationally designed Pt_1Pd single-atom alloy catalyst enables high-performance Li–O_2 batteries. J. Am. Chem. Soc. **146**(4), 2339–2344 (2024). https://doi.org/10.1021/jacs.3c12734
29. L. Li, M. Hua, J. Li, P. Zhang, Y. Nie et al., Tuning dual catalytic active sites of Pt single atoms paired with high-entropy alloy nanoparticles for advanced Li–O_2 batteries. ACS Nano **19**(4), 4391–4402 (2025). https://doi.org/10.1021/acsnano.4c12499
30. X. Hu, G. Luo, Q. Zhao, D. Wu, T. Yang et al., Ru single atoms on N-doped carbon by spatial confinement and ionic substitution strategies for high-performance Li–O_2 batteries. J. Am. Chem. Soc. **142**(39), 16776–16786 (2020). https://doi.org/10.1021/jacs.0c07317
31. D. Du, H. He, R. Zheng, L. Zeng, X. Wang et al., Single-atom immobilization boosting oxygen redox kinetics of high-entropy perovskite oxide toward high-performance lithium–oxygen batteries. Adv. Energy Mater. **14**(17), 2304238 (2024). https://doi.org/10.1002/aenm.202304238
32. P. Wang, Y. Ren, R. Wang, P. Zhang, M. Ding et al., Atomically dispersed cobalt catalyst anchored on nitrogen-doped carbon nanosheets for lithium–oxygen batteries. Nat. Commun. **11**(1), 1576 (2020). https://doi.org/10.1038/s41467-020-15416-4
33. L.-N. Song, W. Zhang, Y. Wang, X. Ge, L.-C. Zou et al., Tuning lithium-peroxide formation and decomposition routes with single-atom catalysts for lithium–oxygen batteries. Nat. Commun. **11**(1), 2191 (2020). https://doi.org/10.1038/s41467-020-15712-z
34. P. Wang, D. Zhao, X. Hui, Z. Qian, P. Zhang et al., Bifunctional catalytic activity guided by rich crystal defects in Ti_3C_2 MXene quantum dot clusters for Li–O_2 batteries. Adv. Energy Mater. **11**(32), 2003069 (2021). https://doi.org/10.1002/aenm.202003069
35. D. Zhang, G. Zhang, R. Liu, R. Yang, X. Li et al., Mutually activated 2D $Ti_{0.87}O_2$/MXene monolayers through electronic compensation effect as highly efficient cathode catalysts of Li–O_2 batteries. Adv. Funct. Mater. **35**(5), 2414679 (2025). https://doi.org/10.1002/adfm.202414679
36. X. Zheng, M. Yuan, Y. Zhao, Z. Li, K. Shi et al., Status and prospects of MXene-based lithium–oxygen batteries: theoretical prediction and experimental modulation. Adv. Energy Mater. **13**(20), 2204019 (2023). https://doi.org/10.1002/aenm.202204019
37. X.-W. Lv, J. Gong, S. Wang, X. Yan, C. Sun et al., Engineering orbital hybridization in advanced electrocatalysts for energy conversion: fundamentals, modulations, and perspectives. Adv. Energy Mater. **15**(30), 2501129 (2025). https://doi.org/10.1002/aenm.202501129
38. L. Chen, J. Xia, Z. Lai, D. Wu, J. Zhou et al., Coordinatively unsaturated co single-atom catalysts enhance the performance of lithium-sulfur batteries by triggering strong d–p orbital

hybridization. ACS Nano **18**(45), 31123–31134 (2024). https://doi.org/10.1021/acsnano.4c08728

39. X. Leng, K. Yang, L. Sun, J. Weng, J. Xu, Modulating the band structure of two-dimensional black phosphorus via electronic effects of organic functional groups for enhanced hydrogen production activity. Angew. Chem. Int. Ed. **64**(5), e202416992 (2025). https://doi.org/10.1002/anie.202416992
40. K. Chen, Y. Zhu, Z. Huang, B. Han, Q. Xu et al., Strengthened d–p orbital hybridization on metastable cubic Mo_2C for highly stable lithium–sulfur batteries. ACS Nano **18**(51), 34791–34802 (2024). https://doi.org/10.1021/acsnano.4c11701
41. S. Cai, M. Zheng, X. Lin, M. Lei, R. Yuan et al., A synergistic catalytic mechanism for oxygen evolution reaction in aprotic Li–O_2 battery. ACS Catal. **8**(9), 7983–7990 (2018). https://doi.org/10.1021/acscatal.8b02236
42. T. Zhang, B. Zou, X. Bi, M. Li, J. Wen et al., Selective growth of a discontinuous subnanometer Pd film on carbon defects for Li–O_2 batteries. ACS Energy Lett. **4**(12), 2782–2786 (2019). https://doi.org/10.1021/acsenergylett.9b02202
43. K. Song, J. Jung, M. Park, H. Park, H.-J. Kim et al., Anisotropic surface modulation of Pt catalysts for highly reversible Li–O_2 batteries: high index facet as a critical descriptor. ACS Catal. **8**(10), 9006–9015 (2018). https://doi.org/10.1021/acscatal.8b02172
44. J. Tian, Y. Rao, W. Shi, J. Yang, W. Ning et al., Sabatier relations in electrocatalysts based on high-entropy alloys with wide-distributed d-band centers for Li–O_2 batteries. Angew. Chem. Int. Ed. **62**(44), e202310894 (2023). https://doi.org/10.1002/anie.202310894
45. Y. Zhou, Q. Gu, K. Yin, L. Tao, Y. Li et al., Cascaded orbital-oriented hybridization of intermetallic Pd_3Pb boosts electrocatalysis of Li–O_2 battery. Proc. Natl. Acad. Sci. U.S.A. **120**(25), e2301439120 (2023). https://doi.org/10.1073/pnas.2301439120
46. Q. Lv, Z. Zhu, Y. Ni, B. Wen, Z. Jiang et al., Atomic ruthenium-riveted metal-organic framework with tunable d-band modulates oxygen redox for lithium–oxygen batteries. J. Am. Chem. Soc. **144**(50), 23239–23246 (2022). https://doi.org/10.1021/jacs.2c11676
47. Y. Rao, J. Yang, J. Tian, W. Ning, S. Guo et al., The spin-selective channels in fully-exposed PtFe clusters enable fast cathodic kinetics of Li–O_2 battery. Angew. Chem. Int. Ed. **64**(7), e202418893 (2025). https://doi.org/10.1002/anie.202418893
48. H. Xu, X. Wang, G. Tian, F. Fan, X. Wen et al., Manipulating electron delocalization of metal sites *via* a high-entropy strategy for accelerating oxygen electrode reactions in lithium–oxygen batteries. ACS Nano **18**(40), 27804–27816 (2024). https://doi.org/10.1021/acsnano.4c11909